Chapter-4

Compositional effect on oxygen reduction reaction in Pr excess double perovskite $Pr_{1+x}Ba_{1-x}Co_2O_{6-\delta}$ cathode materials

Publication: ***Ajay S. Bangwal, Pardeep K. Jha, Manisha Chauhan, Sikha Singh, A.S.K. Sinha, Priyanka A. Jha and Prabhakar singh***, *Int. J. Hydrogen Energy, vol. 45, no. 43, pp. 23378–23390, 2020, doi: 10.1016/j.ijhydene.2020.06.087.*

CHAPTER 4: Compositional effect on Oxygen reduction reaction in Pr excess double perovskite $Pr_{1+x}Ba_{1-x}Co_2O_{6-\delta}$ cathode materials

4.1 Introduction

The performance of the cells basically depends on the electrodes and electrolytes characteristics. In case of the electrodes, porosity, electronic conduction, ORR and OER processes are essential norms. In the chapter 3, the electronic conduction and porosity of the sample PBCO has been studied in detail. In addition, the ORR processes are studied using electro catalysis. Also, electrode polarization losses associated with the triple phase boundary is also one of the focus areas for investigation[144], [145]. For ORR, better performance and reduced polarization losses, mixed ionic-electronic cathode (MIEC) with larger surface area are used[145], [146]. Hence, the parameters such as composition, area and thickness etc. becomes important to tailor the properties of cathode.

The electrodes are basically governed by the electron transfer and the energy of electrons can be modified on application of voltage across the electrode. At the same time, the corrosion of electrodes decreases the performance with time and its rate depends on the electrode, electrolyte and operating temperature. With the increase in temperature, the cathodes degrade rapidly and several electrodes degrade even at room temperature due to mechanical strain or the disintegration of bonding material. The electrochemical interactions of the electrodes need to be investigated to study the degradation and performance at the triple phase boundary (TPB). At the TPB, the surface interactions are being driven by one

electron transfer, two step and 4-step reactions through the alteration of the driving force of a reaction and control of the thermodynamic and kinetic factors.

It is also reported that oxygen kinetics is much faster in layered order perovskite than that of the disordered Perovskites[147]. Layered oxygen deficient cobalt Perovskites $LnBaCo_2O_{6-\delta}$ (where Ln= La, Pr, Gd, Sm, and Y) have drawn interest due to the variable oxidation states of Co with the oxygen deficiency, δ. Amongst the various $LnBaCo_2O_{6-\delta}$ (LnBCo) $PrBaCo_2O_{6-\delta}$ (PBCO) is one of the most promising cathode materials for SOFC[148]. As reported earlier, PBCO exhibited best cathodic performance in LnBCO (where Ln = La, Pr, Gd, Sm, and Y) due to more A site order to form the more oxygen vacancy structures[149], [150]. It is also observed that 'A' site ordering and morphology change enhances oxygen ion diffusivity in bulk materials[151]. In the chapter 3, we have also observed that the PBCO has higher electronic conductivity and its bulk form is more stable than its nano form. But it was found that the samples get corroded during cyclic voltammetry (electrocatalysis) measurement. Therefore, the effect of compositional variation (Pr/Ba ratio in $Pr_{1+x}Ba_{1-x}Co_2O_{6-\delta}$) on the physico-chemical behaviour is investigated in this chapter.

As mentioned in chapter 1, the effect of substitution on the kinetics of ORR is least studied. In addition, the electrode materials dissolute at the triple phase boundary and most importantly PBCO based materials are not studied so far. Thus, ratio of A site cations is varied to form (1+x) $PrCoO_3$-(1-x) $BaCoO_3$ (a Pr rich series $Pr_{1+x}Ba_{1-x}Co_2O_{6-\delta}$ (x= 0.0, 0.2, 0.4, 0.6, 0.8 and 1.0)) using conventional solid-state route. During the catalytic experiments, a very fast electrochemical reaction occurred in case of the above synthesized composite materials and more hydrogen gas liberated than oxygen gas during the surficial reactions at

TPB. The triple phase boundary reactions suggest the formation of $Co(OH)_3$ on reaction of these composite electrodes with H_2O during electrochemical dissolution.

4.2 Experimental Procedure

4.2.1 Synthesis

The series $Pr_{1+x}Ba_{1-x}Co_2O_{6-\delta}$ (here mentioned as (1+x) $PrCoO_3$-(1-x) $BaCoO_3$) with compositions $Pr_{1+x}Ba_{1-x}Co_2O_{6-\delta}$, x = 0.0 - 1.0 at the step of 0.2 were synthesized using solid-state reaction route. The precursors Pr_6O_{11} (99.5 %), $BaCO_3$ (99 %) and Co_3O_4 (99.7 %) from M/s Alfa- Aesar were weighed in stoichiometric amounts to get the desired compositions. The mixtures were wet ground with agate mortar in acetone medium for 5-6 h. The samples were then calcined at 1000 ^oC for 10 h. The samples were ground again and pelletized uniaxially using hydraulic press by applying pressure of 4-5 kg/m^2. The diameter of the samples was about 12-13 mm and the thickness was maintained 1-2 mm. The pelletized samples were then sintered at 1050 ^oC for 10 h[152]. The heating rate for both the calcination and sintering process was maintained at 5 ^oC/ minute.

4.2.2 Characterization technique

The details of all the characterization techniques including XRD, SEM, EDX, XPS and CV is already mentioned in chapter 2. For Cyclic voltammetry, 1 M solution of Sodium sulfate (Na_2SO_4) was used as an electrolyte. Ag/AgCl electrode stored in 1 M KCl solution, was used as a reference and Pt wire as counter electrodes. (1+x) $PrCoO_3$-(1-x) $BaCoO_3$ were used as working electrode directly. CV was performed with scan rates of 30, 50, 70, 100, 150, 200 and 250 mV/sec. The Tafel Slope was calculated on Linear scale voltammetry (LSV) curves by plotting the Potential against log (current density).

4.3 Results and Discussion

4.3.1 Tolerance factor

It is known that Co has variable oxidation states with high spin (HS), low spin (LS) and intermediate spin (IS) configurations, thus Goldschmidt tolerance factor (t) is calculated (Fig.5.1). The tolerance factor is observed to decrease with the increase in $PrCoO_3$ content and is lowest for $PrCoO_3$. The value of tolerance factor for the studied compositions is less than 1 for Co^{2+} (LS) and Co^{2+} (HS) configurations, while the compositions with other Co configurations have tolerance factor greater than 1. Co^{3+} (LS) and Co^{4+} (LS) configurations are observed to have tolerance factor greater than 1 for the studied compositions. In case of Co^{3+} (HS) configuration, tolerance factor decreases from 1.0095 to 0.9308 with x. It is observed earlier that $PrBaCo_2O_{6-\delta}$ and $PrCoO_3$ are found in orthorhombic phase and for orthorhombic phase tolerance factor lies between 0.8-1. Thus, for the orthorhombic phase, Co should occur in Co^{2+} (LS) state.

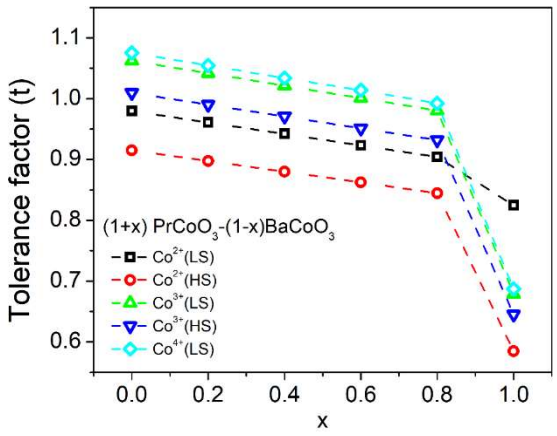

Figure 4.1: Tolerance factor of the studied compositions (1+x) $PrCoO_3$ - (1-x) $BaCoO_3$

4.3.2 Structural and microstructural studies

$PrCoO_3$ and $BaCoO_3$ are known to have orthorhombic structure with P*nma* symmetry[148] and hexagonal structure with P*63/mmc* symmetry respectively[153], while room temperature structure of $PrBaCo_2O_{6-\delta}$ is reported to be orthorhombic with P*mmm* symmetry[152]. In the present case, XRD has been done to analyze the phase formation and the interaction of two structures. It can be seen in Fig.4.2 that a peak at $2\theta \sim 33.5^o$ starts to appear for $x \geq 0.2$ and its intensity gradually increases with the increase in x. Finally at x = 1.0 i.e., for $PrCoO_3$, the maximum intense peaks at $2\theta \sim 32^o$ disappear and the above mentioned peaks corresponding to $2\theta \sim 33.5^o$ maximise. Some peaks are observed at x = 1.0 in addition to the indexed peaks corresponding to Pr_2O_3 (#47-1111). This peak has been indexed as (121) according to the Rietveld refinement of $PrCoO_3$ studied later. The peak (022) according to indexing of x = 0.0 i.e. $PrBaCo_2O_{6-\delta}$ is observed to have right angle shifting with x. In addition, the other two peaks (100) and (022) at $2\theta \sim 24^o$ merge to a single peak with indexing (101) at $2\theta \sim 24^o$ for x = 1.0. Thus, with the increase in x, two structures are observed to co-exist. Rietveld refinement has been done using double phase pcr file (Fig. 4.2) comprising of two symmetries one of $PrBaCo_2O_{6-\delta}$ (P*mmm*) and other of $PrCoO_3$ (P*nma*). The value of R-factor and χ^2 lies within appreciable range for all the samples. All the parameters obtain through Rietveld refinement are listed in table 4.1.

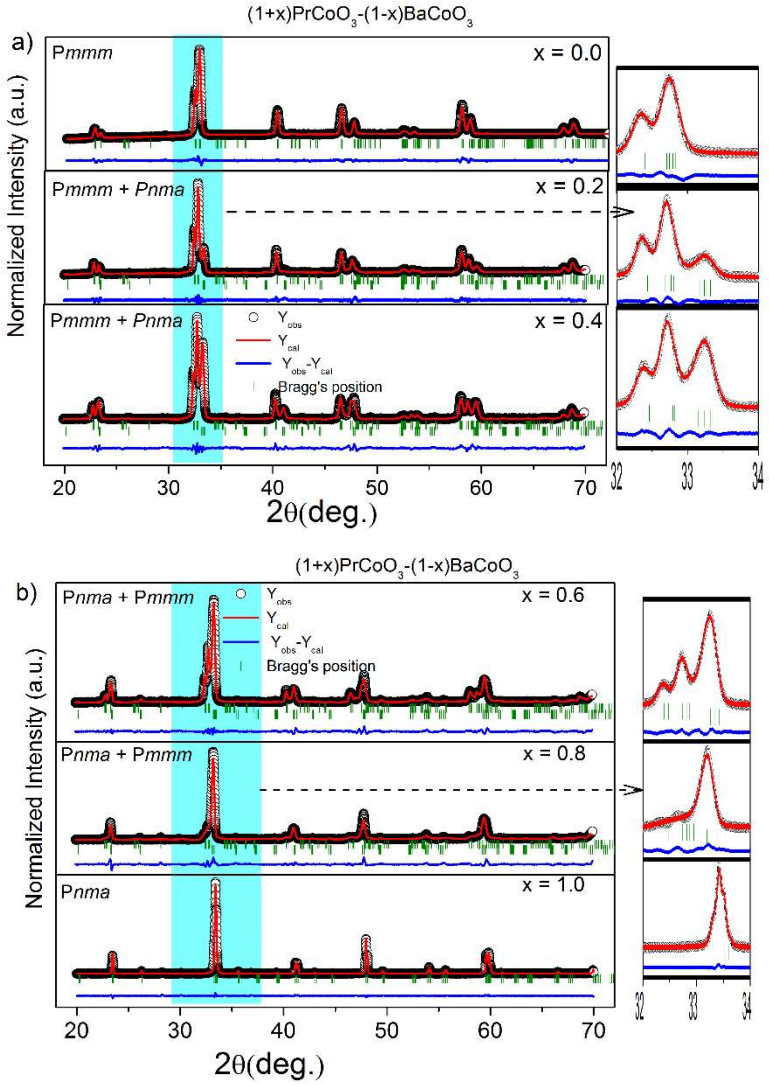

Figure 4.2: (a, b) Rietveld refined X-ray diffraction patterns of the studied compositions (1+x) $PrCoO_3$ - (1-x) $BaCoO_3$

The individual phase % obtained from the Rietveld refinement is shown in Fig.4.3(a). The amount of phase 1 corresponding to P*mmm* symmetry is observed to decrease continuously. Simultaneously, amount of phase 2 corresponding to P*nma* symmetry is observed to increase. The lattice parameters 'b' corresponding to Pmmm phase is observed to have a broad minimum at x = 0.4 and x= 0.6. Whereas, the lattice parameter 'b'

corresponding to P*nma* phase is observed to continuously increase and have a minimum value at x =1.0 (Fig. 4.3(b)). This variation of lattice parameters is observed due to the orthorhombic distortion (O.D. = (a-b)/(a+b)), as depicted in inset of Fig.4.3(b). Orthorhombic distortion is observed to follow the same trend as lattice parameter 'b'. On a comparative note, distortion in double perovskite $PrBaCo_2O_{6-\delta}$ (x = 0.0) is higher than single perovskite $PrCoO_3$ (x = 1.0).

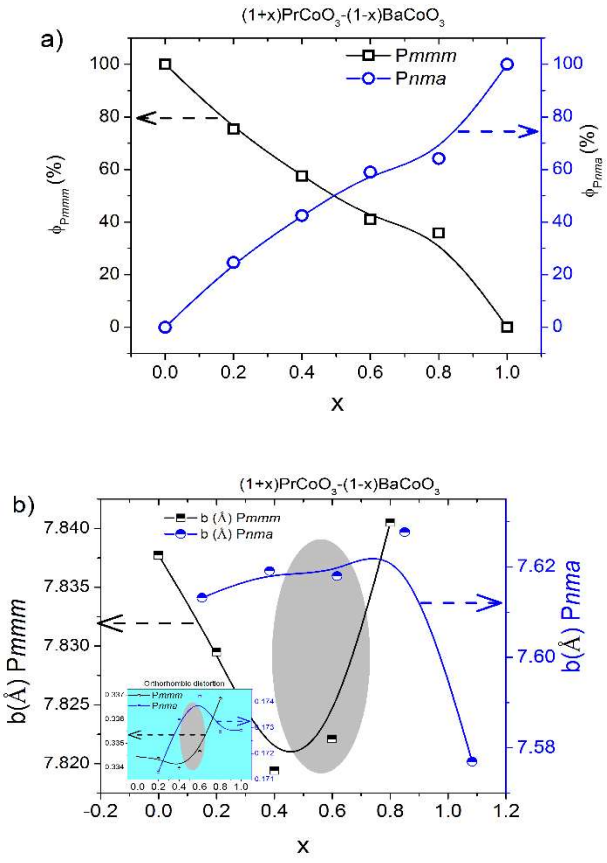

Figure 4.3: (a) Phase % of $PrBaCo_2O_{6-\delta}$ (φ_{Pmmm}) and $PrCoO_3$ (φ_{Pnma}) (b) Lattice parameter 'b' corresponding to $PrBaCo_2O_{6-\delta}$ (φ_{Pmmm}) and $PrCoO_3$ (φ_{Pnma}) (b, inset) Orthorhombic distortion $PrBaCo_2O_{6-\delta}$ (φ_{Pmmm}) and $PrCoO_3$ (φ_{Pnma})

Sample	Phase	Lattice parameters	Atoms	x	y	z	R - factors
x = 0	P*mmm*	a = 3.90915 Å	Ba	0.5	0.25089	0	R_P = 10.0 R_{WP} = 6.56 R_{Bragg} = 2.06 R_F = 4.09 $\chi 2$ = 1.43
		b = 7.83773 Å	Pr	0.5	0.25863	0.5	
		c = 7.64173 Å	Co1	0	0.5	0.25272	
			Co2	0	0	0.24319	
			O1	0	0	0	
			O2	0	0.5	0	
			O3	0	0.5	0.5	
			O4	0	0	0.5	
			O5	0.5	0	0.24699	
			O6	0.5	0.5	0.25567	
			O7	0	0.25721	0.31407	
x = 0.2	P*mmm*	a = 3.9055 Å	Ba	0.5	0.24938	0	R_P = 15.9 R_{WP} = 11.1 R_{Bragg} = 4.25 R_F = 5.92 $\chi 2$ = 3.31
		b = 7.8295 Å	Pr	0.5	0.24889	0.5	
		c = 7.66 Å	Co1	0	0.5	0.25068	
			Co2	0	0	0.21856	
			O1	0	0	0	
			O2	0	0.5	0	
			O3	0	0.5	0.5	
			O4	0	0	0.5	
			O5	0.5	0	0.21934	
			O6	0.5	0.5	0.22983	
			O7	0	0.33295	0.2057	
	P*nma*	a = 5.3864 Å	Pr	0.02258	0.25	0.52505	R_P = 15.9 R_{WP} = 11.1 R_{Bragg} = 10.6 R_F = 10.6 $\chi 2$ = 3.31
		b = 7.6132 Å	Ba	0.02258	0.25	0.52505	
		c = 5.3959 Å	Co	0	0	0	
			O1	1.45791	0.25	0.95456	Phase1 = 75.33%, Phase2 =24.67%
			O2	0.70199	0.47054	0.76627	
x = 0.4	P*mmm*	a = 3.9041 Å	Ba	0.5	0.25184	0	

		b = 7.8194 Å	Pr	0.5	0.25399	0.5	R_P = 13.9 R_{WP} = 10.3 R_{Bragg} = 4.32 R_F = 5.28 $\chi 2$ = 3.38
		c = 7.6555 Å	Co1	0	0.5	0.21452	
			Co2	0	0	0.25117	
			O1	0	0	0	
			O2	0	0.5	0	
			O3	0	0.5	0.5	
			O4	0	0	0.5	
			O5	0.5	0	0.22013	
			O6	0.5	0.5	0.2261	
			O7	0	0.03237	0.11151	
	P*nma*	a = 5.3684 Å	Pr	0.02046	0.25	0.50919	R_P = 13.9 R_{WP} = 10.3 R_{Bragg} = 5.27 R_F = 5.86 $\chi 2$ = 3.38
		b = 7.6191 Å	Ba	0.02046	0.25	0.50919	
		c = 5.3994 Å	Co	0	0	0	
			O1	1.75561	0.25	0.98841	Phase1 = 57.57%, Phase2 =42.43%
			O2	0.8598	0.4598	0.81799	
x = 0.6	P*mmm*	a = 3.8993 Å	Ba	0.5	0.25603	0	R_P = 16.0 R_{WP} = 11.2 R_{Bragg} = 8.06 R_F = 9.53 $\chi 2$ = 3.77
		b = 7.8221 Å	Pr	0.5	0.25894	0.5	
		c = 7.6439 Å	Co1	0	0.5	0.22571	
			Co2	0	0	0.24301	
			O1	0	0	0	
			O2	0	0.5	0	
			O3	0	0.5	0.5	
			O4	0	0	0.5	
			O5	0.5	0	0.25337	
			O6	0.5	0.5	0.22928	
			O7	0	0.33336	0.03117	
	P*nma*	a = 5.3573 Å	Pr	0.00072	0.25	0.4956	R_P = 16.0 R_{WP} = 11.2 R_{Bragg} = 5.68 R_F = 8.60 $\chi 2$ = 3.77
		b = 7.618 Å	Ba	0.00072	0.25	0.4956	
		c = 5.4022 Å	Co	0	0	0	

			O1	1.62407	0.25	0.97832	Phase1 = 40.97%, Phase2 =59.03%
			O2	0.88712	0.44893	0.82148	
x = 0.8	P*mmm*	a = 3.8892 Å	Ba	0.5	0.25603	0	R_P = 20.0 R_{WP} = 17 R_{Bragg} = 3.61 R_F = 3.11 $\chi 2$ = 8.83
		b = 7.8405 Å	Pr	0.5	0.25984	0.5	
		c = 7.6265 Å	Co1	0	0.5	0.22571	
			Co2	0	0	0.24301	
			O1	0	0	0	
			O2	0	0.5	0	
			O3	0	0.5	0.5	
			O4	0	0	0.5	
			O5	0.5	0	0.25337	
			O6	0.5	0.5	0.22928	
			O7	0	0.33336	0.03117	
	P*nma*	a = 5.3794 Å	Pr	0.00254	0.25	0.51632	R_P = 20.0 R_{WP} = 17 R_{Bragg} = 7.66 R_F = 6.21 $\chi 2$ = 8.83
		b = 7.6277 Å	Ba	0.00254	0.25	0.51632	
		c = 5.4055 Å	Co	0	0	0	
			O1	1.93528	0.25	0.97629	Phase1 = 35.86%, Phase2 =64.14%
			O2	0.94215	0.48103	0.22211	
x = 1.0	P*nma*	a = 5.34281 Å	Pr	0.02945	0.25	1.50875	R_P = 12.6 R_{WP} = 7.66 R_{Bragg} = 2.48 R_F = 3.03 $\chi 2$ = 1.99
		b = 7.57693 Å	Co	0	0	0	
		c = 5.37716 Å	O1	0.01004	0.25	-1.9562	
			O2	1.68972	0.01398	0.30966	

Table 4.1: Rietveld refinement parameter of (1+x) $PrCoO_3$ - (1-x) $BaCoO_3$

To illustrate the double phase formation of the studied compositions (1+x) $PrCoO_3$ - (1-x) $BaCoO_3$, we have estimated specific heat using DSC (Fig. 4.4). According to the relation $C_V = C_{el} + C_{ph} = \gamma T + \beta T^3$ where $\gamma = (2/3)\pi k_B{}^2 N(E_F)$ and $\beta = 12\pi^4 N_A k_B / 5\Theta_D{}^3$. Here we have used N = N_A, Avogadro number, $N(E_F)$ is density of states at Fermi level, and Θ_D is Debye temperature. C_v data is fitted with this equation and fitting gives the $N(E_F)$ corresponding to the density of states (DOS) of a single phase. It can be seen that the Schottky anomaly comprises of two peaks rather than one. These two peaks correspond to the different DOS corresponding to the two phases. Moreover, it is also seen that at x = 0.6 and x= 0.8, the DOS of the two phases is nearly equal. While at x = 1.0, the fitting has been achieved with a single peak. Hence, composite phase is confirmed from the XRD and DSC measurements.

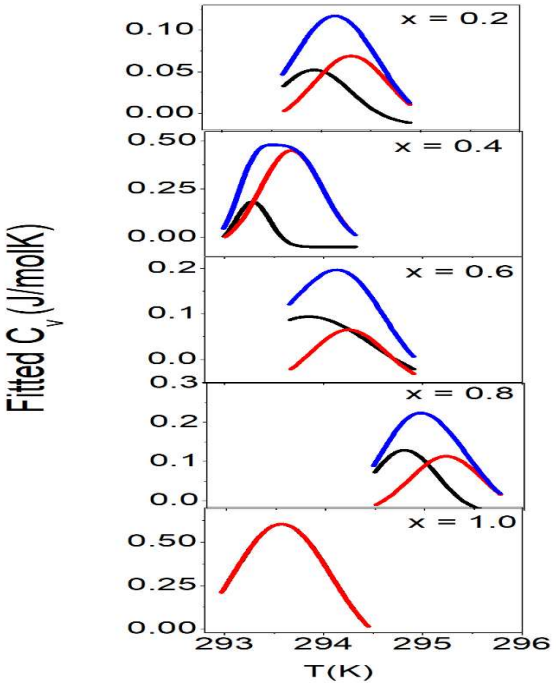

Figure 4.4: Specific heat (C_v) of the studied compositions (1+x) $PrCoO_3$ - (1-x) $BaCoO_3$ showing the presence of two phases $PrBaCo_2O_{6-\delta}$ and $PrCoO_3$

For the cathode applications, oxygen has to traverse across grains and along grain boundary. The porous electrodes become a criterion as they provide abundant sites for electrochemical reactions and an easy pathway for oxygen gas to transport to the electrolyte. To understand grain morphology, SEM images of all the sintered samples are studied (Fig. 4.5). The porous and well-connected grains are observed up to x = 0.4. Further, grain size reduces at x = 0.6 and x= 0.8. Finally, morphology of grain changes at x = 1.0. But the SEM micrographs do not reveal any composite feature in the studied compositions.

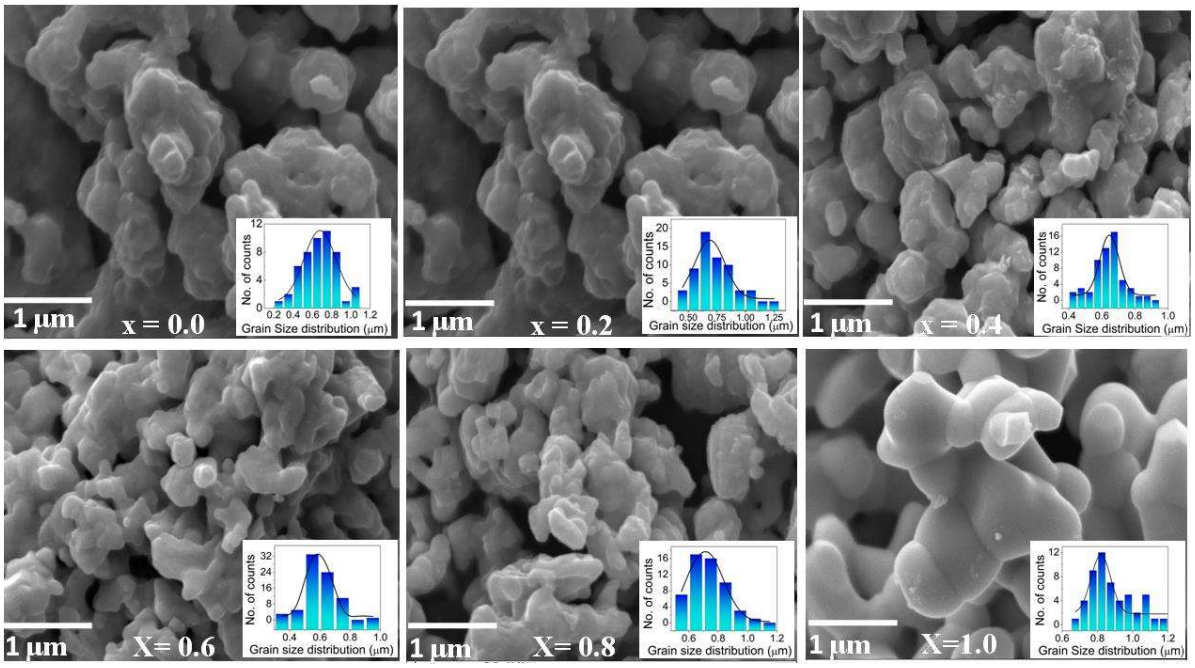

Figure 4.5: SEM micrographs and respective grain size histograms of (1+x) $PrCoO_3$ - (1-x) $BaCoO_3$

The density of the (1+x) $PrCoO_3$ - (1-x) $BaCoO_3$ (x = 0.2, 0.4, 0.6 and 0.8) compositions has been obtained using Archimedes' kit (Fig.4.6). Further, porosity has been estimated using equation 4.1:

$$Porosity\ (\%) = \left(1 - \left(\frac{exp.density}{th.density}\right)\right) * 100 \qquad (4.1)$$

It is found that porosity is maximum ~35 % for composition with x = 0.6, which can be correlated with open pores and reduced grain size observed in the SEM image.

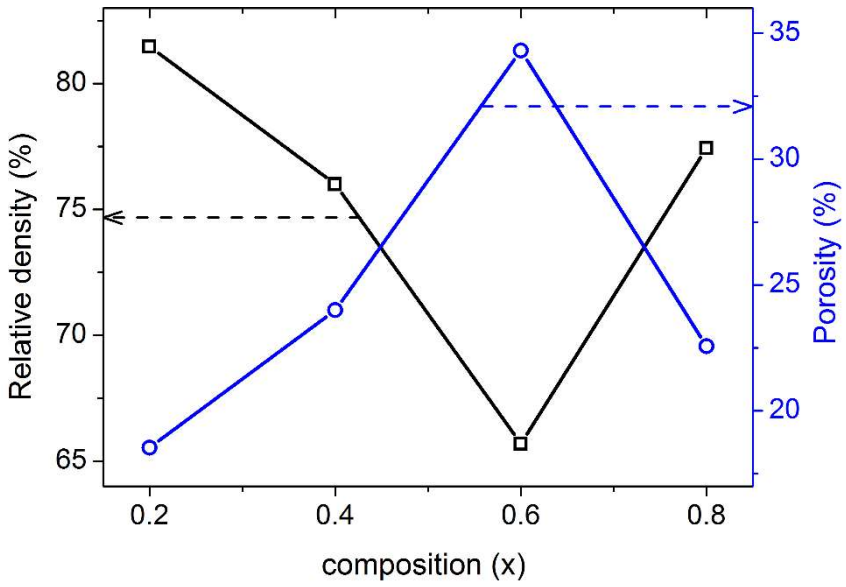

Figure 4.6: Density and Porosity measured through Archimedes' principle of (1+x) $PrCoO_3$ - (1-x) $BaCoO_3$ (x = 0.2, 0.4, 0.6 and 0.8)

4.3.3 X-ray photoelectron spectroscopy studies

For the chemical compositions, elemental concentration and variable oxidation states, XPS measurements have been performed. The elemental spectra of all the samples were calibrated with respect to the standard Carbon peak C1s appearing at 284.6 eV. Fig.4.7 shows the deconvoluted XPS spectra using XPS peak 4.1 of Pr3d, Co2p and O1s with Shirley background. According to standard XPS fitting, in Pr 3d spectra, $Pr3d_{5/2}$ and $Pr3d_{3/2}$ peaks occur along with two respective satellites. At x = 0.0, Pr spectra is observed in accordance with the predicted ones. But with the increase in $PrCoO_3$ content, the satellite peak merges in Pr $3d_{3/2}$ peak and the intensity of satellite peak are increasing with x. Simultaneously, Co XPS spectra is matching with the standard i.e., showing $2p_{3/2}$ and $2p_{1/2}$ peaks along with the respective satellites and the presence of Co^{3+} and Co^{4+} oxidation states. At x = 0.4, the

satellite peaks are missing but Co^{2+} oxidation state is seen along with Co^{3+} and Co^{4+} states. For x > 0.4, the satellite peaks again appear with the co-existence of three states and deconvoluted peak intensity corresponding to Co^{2+} is observed to increase. In addition, deconvoluted XPS spectra corresponding to O 1s is known to exhibit metal-O, metal-hydroxide and auger peaks as observed for x = 0.0. But with the increase in x, intensity corresponding to metal-O is observed to increase instead of the hydroxide bond intensity. Metal-O peak represents the oxygen vacancy and Metal – hydroxide represents the vacancy adsorbed. Hence, in the present case, vacancy is more than the adsorbed oxygen for x = 1.0. The samples become more oxygen deficient and the deficiency, δ, estimated using XPS is matching with the EDX data and is equal to 0.4 for x = 0.0. Most importantly, the width of Pr $3d_{5/2}$ convoluted peak remains the same but the satellite peak width and Pr $3d_{3/2}$ changes with x. In addition, nearly no displacement is observed in Co peaks rather than the displacement is observed in Pr and O peak showing the change in oxidation state from Pr^{3+} to $Pr^{3+\delta}$ and O^{-2} to $O^{-2-\delta}$[154], [155]. The elemental concentration obtained from XPS peak fitting is matching with the elemental concentration with EDX. Here, the satellite peaks of Pr and Co are interacting with the auger peaks of O showing the transfer of electron and the reduction of oxygen vacancy through the electron consumption as observed through Auger peak. But Co-O bond is not playing a critical role in the mechanism rather than Pr-O bond as observed through the variation of grain size and Pr content (Fig.4.8). The grain size is observed to vary with Pr content instead of O showing the formation of rough grains seen in Fig. 4.5. This can be attributed to the alteration in driving force and chemical potentials associated with the Pr content. This is also observed through the decrease in gap between the grains. Thus, with the variable oxidation states of Pr, Co and O, X-ray diffractograms showed refinement with two

iso-structural symmetries (P*mmm* and P*nma*), simultaneously, SEM micrographs also showed the homogeneous grains (being iso-structural) and composite feature is observed neither in SEM (Fig. 4.5).

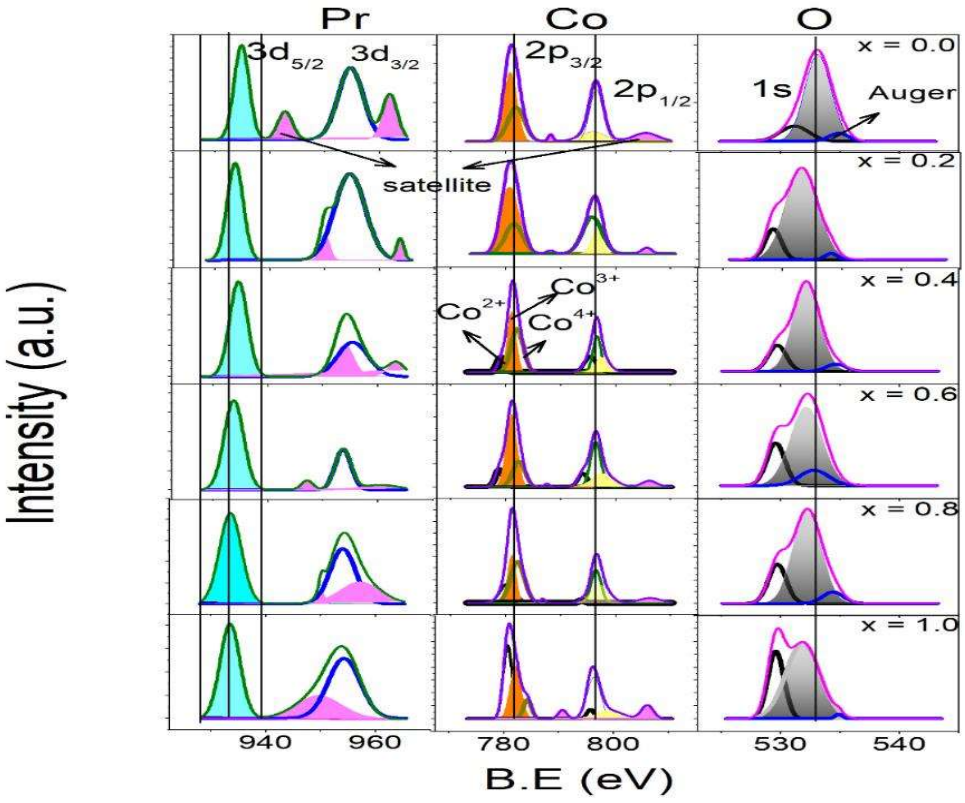

Figure 4.7: Deconvoluted XPS spectra using XPS peak of Pr3d, Co2p and O1s with Shirley background

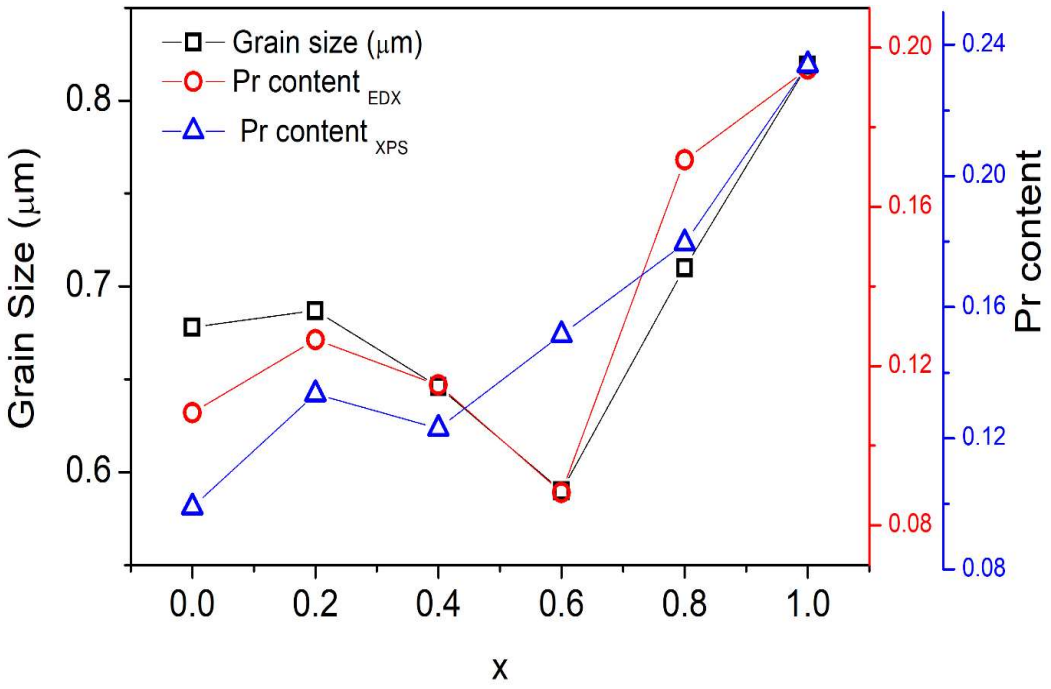

Figure 4.8: Variation of grain size obtained from Grain size histograms and Pr content observed from EDX and XPS with x

4.3.4 Catalytic studies

An electrode is basically an electrical conductor and so far, we have studied that $PrBaCo_2O_{6-\delta}$ is highly conducting that multimeter gives the beep sound like a good conductor and its resistance is less than silver as measured through multimeter. In the present case, the series prepared is also highly conducting like the parent compound x = 0.0. The major criterion for an electrode is being achieved by these samples. Also, an electrode should have high ORR and high cathodic current. In the present case, the electron transfer phenomenon is studied employing cyclic voltammetry. In cyclic voltammetry, scan rate plays a crucial part. For this, we measured the current of the samples using scan rate of 30 mV/s (Fig.5.9). Further, various scan rates are employed to analyze the studied samples. It can be seen in Fig.4.9 that the "duck" shaped cyclic voltammetric curve is obtained for x = 0.0, x = 0.6 and

0.8. These duck shaped curves are a signature of catalytic regeneration of reactant near electrode. The cathodic current is higher in sample x= 0.6 sample in comparison with other studied sample.

In addition, the area under the curve is higher for x = 0.6 as compared to the other samples. In addition to "duck" shaped feature, a kink is also present in the curves showing the existence of multiple oxidation states which are inter-convertible through the electron transfer[111], [156]. The peak voltage and peak current are higher in x = 0.6. The peak cathodic and anodic current for x = 0.0, 0.6 and 0.8 samples show electrochemical reversibility. While, the absence of duck shaped curve in x = 0.2 and 0.4 samples contribute to the less diffusion of the charge carriers to and fro from the electrode.

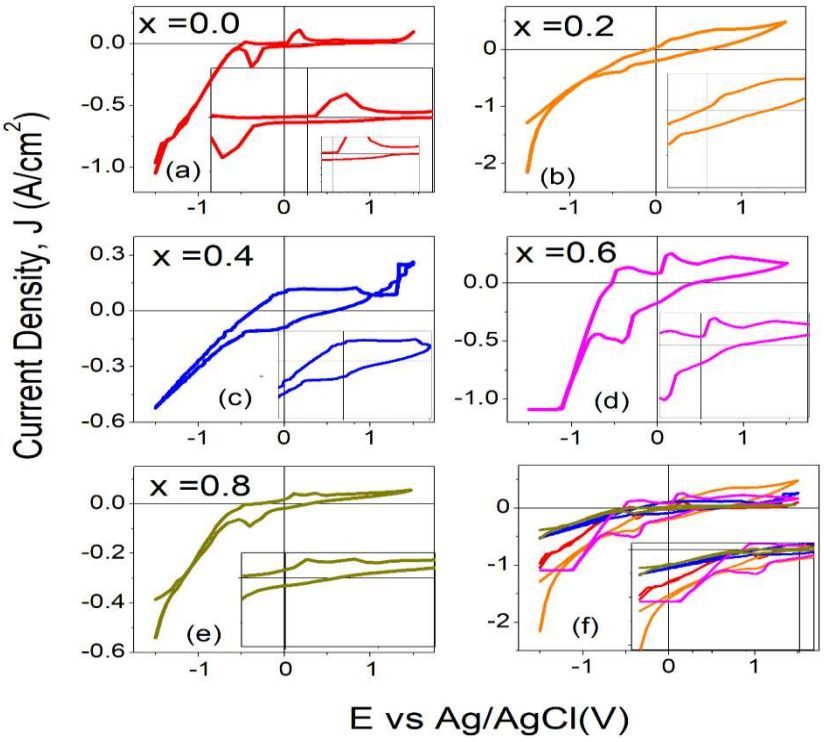

Figure 4.9: Cyclic Voltammetric curves for the (1+x) $PrCoO_3$ - (1-x) $BaCoO_3$ (respective insets) show the area under the curve is higher for x = 0.6, 4th quadrant represents the higher V_{oc} and I_{sc} in x = 0.6 sample

Various scan rates are studied as mentioned in the experimental section to study the diffusion and adsorption mechanisms for the studied sample. Fig. 4.10 depicts the various scan rates for the studied samples. It is observed that with the variation of scan rate, the peak position is observed to shift towards higher current and higher voltages. However, the peaks are not observed for x = 0.2 and x =0.4. The increase in current with the scan rate being a normal observation is basically due to the reduction in the size of diffusion layer with the scan rate[157].

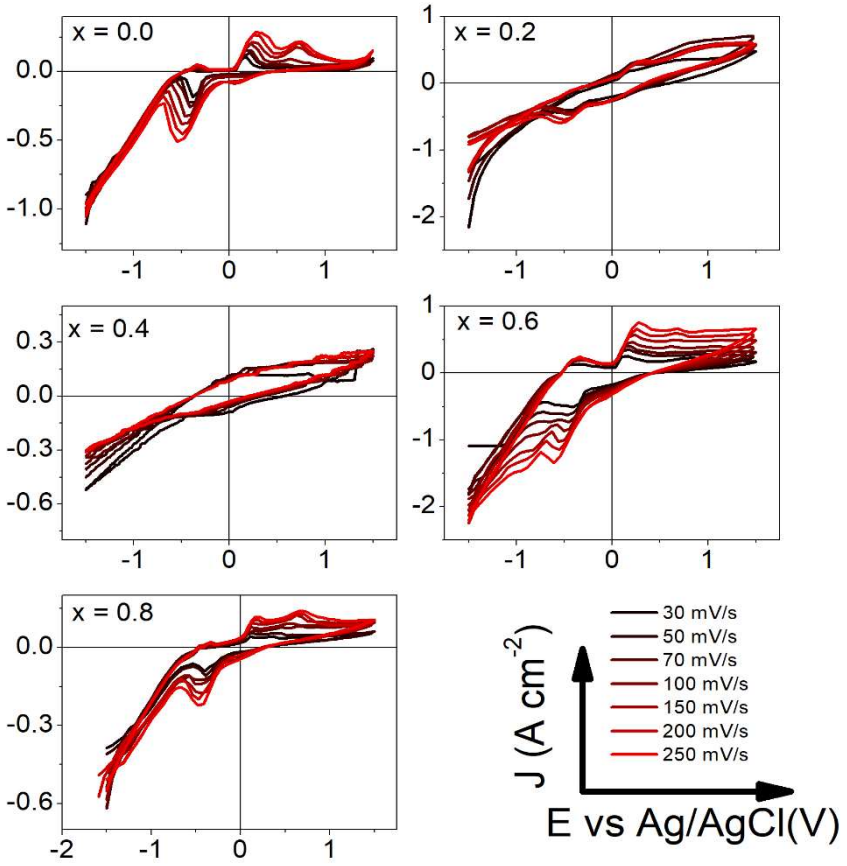

Figure 4.10: Cyclic Voltammetric curves for the (1+x) $PrCoO_3$ - (1-x) $BaCoO_3$ with the different scan rates

To describe peak behavior, Randles-Selvick (RS) equation is used. peak current is plotted versus $v^{1/2}$ (Fig.4.11). For x = 0.0, this plot is nearly linear while for x = 0.2 and x =

0.4, this plot is non-linear for the measured scan rates. But for x = 0.6 and 0.8, it is linear indicating the quasi-electrochemical reversibility with the freely diffusing redox species[157]. In addition, as observed in Fig.5.10, shifting of peak-to-peak separation with the scan rate confirms one electron transfer to and fro between the analyte and the electrode. While, for x = 0.2, 0.4, absence of peaks and non-linear behavior with the scan rate confirms the mixed diffusion adsorption conduction[157].

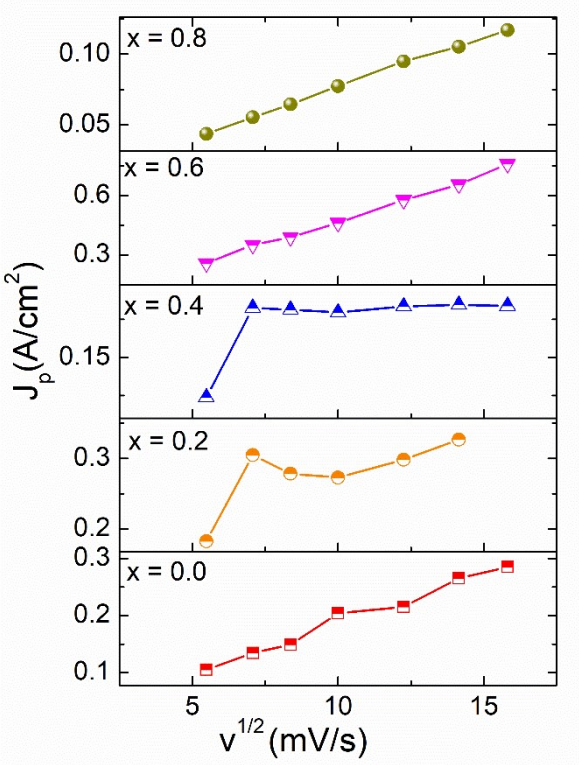

Figure 4.11: Variation of i_p vs $v^{1/2}$ as per RS equation for the (1+x) $PrCoO_3$ - (1-x) $BaCoO_3$

The transient current decay time is estimated from the chronoamperometric response of the (1+x) $PrCoO_3$ - (1-x) $BaCoO_3$ (x = 0.0, 0.6 and x= 0.8) compositions (Fig. 4.12). The transient current decay time is estimated by fitting the current vs time graph (Fig. 4.12) with the exponential decay equation and found to be ~ 703 sec for x = 0.0, ~0.773 sec for x = 0.6

and ~ 326 sec for x = 0.8 compositions. For cathode materials the transient time should be lesser typically of the order of 1 sec. Thus, the sample x = 0.6 is highly suitable for the cathode due to less transient response, electrochemical reversibility with the freely diffusing species.

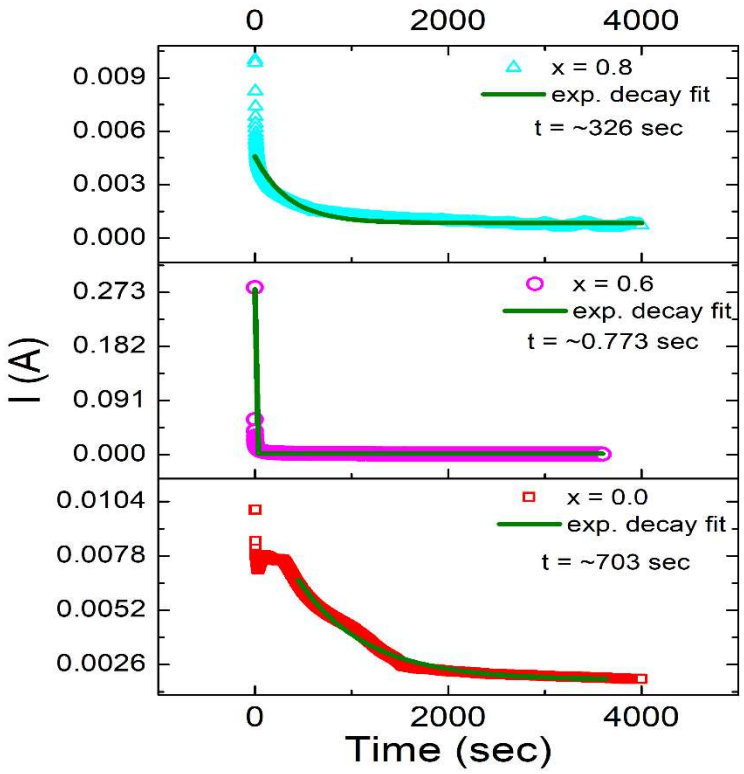

Figure 4.12: Chronoamperometric response for the (1+x) $PrCoO_3$ - (1-x) $BaCoO_3$ (x = 0.0, 0.6 and x= 0.8)

The corrosion rate (CR) is extracted from the Tafel plot. Fig. 4.13 shows the Tafel plot of the (1+x) $PrCoO_3$ - (1-x) $BaCoO_3$ (x = 0.0, 0.6) compositions. It is observed that CR is slightly lower for x = 0.6 (~ 0.10 mm/year) than that for x = 0.0 (~0.11 mm/year). Thus, the sample x = 0.6 is extremely appropriate for the cathode due to less transient response, electrochemical reversibility and less corrosion rate with the freely diffusing species.

As observed earlier, Co is observed to exist in +2, +3 and +4 oxidation states and the shifting of peaks in XPS reveal the change in oxidation states of Pr and O. Further, the grain size is observed to vary with Pr content as Pr-O bond is altering the properties of the studied

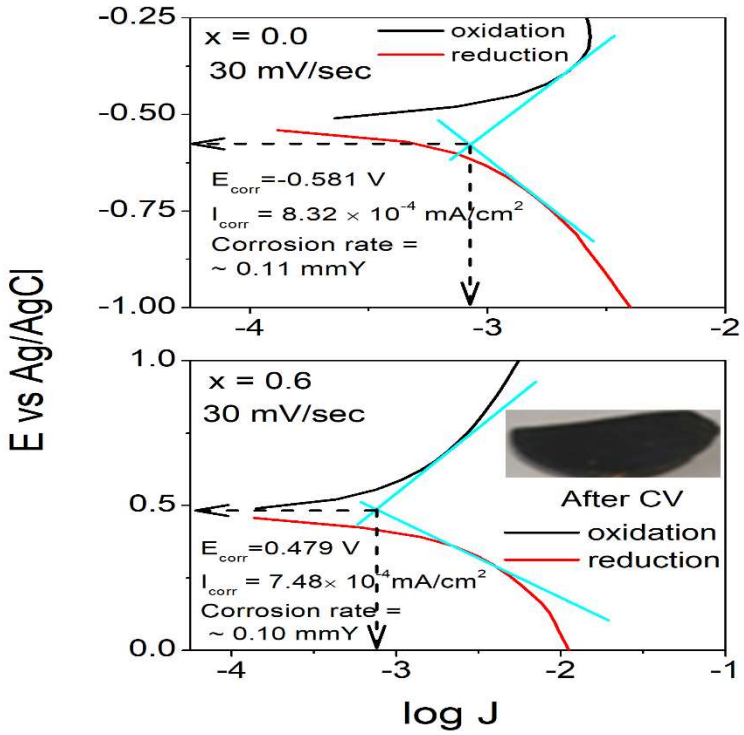

Figure 4.13: Tafel plot showing E_{corr}, I_{corr} and Corrosion rate (CR) of the (1+x) $PrCoO_3$ - (1-x) $BaCoO_3$ (x = 0.0, 0.6) compositions (here corrosion rate in mmY stands for mm/year)

compositions. We have also observed that at x = 0.6, higher ORR is observed in comparison to other substituted samples. In $PrCoO_3$, Co is in +3 oxidation state and in $BaCoO_3$ Co is in +4 oxidation state. With the increase in x, the compositions showed the change in Co oxidation states +2, +3 and +4 as confirmed through XPS (illustrated in equation 4.2).

$$(1+x)PrCoO_3 + (1-x)BaCoO_3 \rightarrow Pr_{1+x}Ba_{1-x}Co_{1+x}Co_{1-x}O_{6-\delta} + \frac{\delta}{2}O_2 \qquad (4.2)$$

Various electrodes like Pt, Pd etc. are known to dissolute and form PtO, PdO on reaction with the H_2O. Similarly, the composite electrodes are also displayed to study the dissolution rate and $Co(OH)_3$ is formed in the present case which is blackish-brown in colour as the sample. The illustration of the formation of $Co(OH)_3$ depends on x which changes the Co in +3 state and shown in equation 4.3. Simultaneously, the formation of H_2 gas depends on the formation of $Co(OH)_3$, the more $Co(OH)_3$ is formed, less will be the production of H_2 gas. This is in turn depends on the formation of Co in +3 state which increases with the increase in Pr content (x). Hence, at x = 0.6 (Pr = 1.6) more catalytic activity leads to more H_2 production.

$$Pr_{1+x}Ba_{1-x}Co_{1+x}Co_{1-x}O_{6-\delta} + 3H_2O \rightarrow Pr_{1+x}Ba_{1-x}Co_{1+x-y}Co_{1-x}O_{6-\delta} + yCo(OH)_3 + \left(\frac{6-3y}{2}\right)H_2 \uparrow + \left(\frac{3-3y-\delta}{2}\right)O_2 \uparrow \qquad (4.3)$$

With the increase in Pr content, O vacancy is altered and the formation of bulk oxygen vacancy (seen from XPS) tends to decrease with the increasing O 2p band center with reference to Fermi level and showing enhanced ORR [158]. Further, at x = 0.6, Ba content 0.4 is critical for band center formation. When Ba > 0.4 and Ba< 0.4, Co^{2+} creates electron traps at the surface which can decrease in conductivity leading to an overall decrease in ORR. Thus, sample x = 0.6 has higher ORR in comparison with other substituted samples. Further, a comparative study of the ORR current for the commercial and well-known electrodes with the present work is presented in Table 4.1.

Sl. No	Sample	Synthesis technique	Electrolyte solution	Current density	Ref.
1	$MnFe_2O_4$	Thermal decomposition	1 M KOH	-7 μA	[159]
2	Pd_{Bulk}	N/A	0.5 M NaOH+ 1 M CH_3OH	1.32mA/cm^2	[160]
3	$Pr_{0.5}Ba_{0.5}MnO_{3-\delta}$	Sol gel method	6 M KOH	0.10 A/cm^2	[161]
4	$PrBaMn_2O_{6-\delta}$	Sol gel method	6 M KOH	0.15 A/cm^2	[161]
5	$LaFeO_{3-\delta}$	Self-Combustion route	1 M KOH	0.27 mA/cm^2	[162]
6	$La_{0.4}Sr_{0.6}FeO_{3-\delta}$	Self-Combustion route	1 M KOH	0.12 mA/cm^2	[162]
7	$SrFeO_{3-\delta}$	Self-Combustion route	1 M KOH	0.10 mA/cm^2	[162]
8	$LaCoO_{3-\delta}$	Co-precipitation Method	3 M KOH	3mA/cm^2	[163]
9	Pt/C	Commercial	0.1M KOH	5.5 mA/cm^2	[164]
10	$Ba_{0.5}Sr_{0.5}Co_{0.5}Fe_{0.2}O_{3-\delta}$	Polymerized complex methods	0.1M KOH	4.5 mA/cm^2	[165]
11	$LaNiO_{3-\delta}$	EDTA citrate complex	0.1M KOH	4mA/cm^2	[166]
12	PBM/C	Facile method	0.1M KOH	5mA/cm^2	[164]
13	H-PBM/C	Facile method with H_2	0.1M KOH	6 mA/cm^2	[164]
14	$PrBaCo_2O_{5.5}$	Sol-gel method	0.1M KOH	40 mA/cm^2	[167]
15	$Pr_{1.6}Ba_{0.4}Co_2O_{6-\delta}$	Solid State reaction route	1 M Na_2SO_4	0.5 A/cm^2	**In this work**

Table 4.2: A comparative of commercial and well-known electrodes with the present work.

4.4 Conclusion

A series of (1+x) $PrCoO_3$ - (1-x) $BaCoO_3$ (x = 0.2 to 1 with step of 0.2) compositions are prepared using conventional solid-state ceramic route. The compositions are observed to be

in double phase (confirmed from XRD and DSC studies) with single morphology as no composite behavior is revealed in the SEM micrographs. At x = 0.6, Ba content 0.4 is critical for band center formation and decreases the bulk oxygen vacancy and increases ORR with the higher Pr content. When Ba > 0.4 and Ba< 0.4, Co^{2+} creates electron traps at the surface which can decrease in conductivity leading to an overall decrease in ORR. Thus, sample x = 0.6 has higher ORR with the more production of H_2 gas in comparison with other substituted samples. So, in this chapter we found that the electrode sample $Pr_{1.6}Ba_{0.4}Co_2O_{6-\delta}$ seems to be more promising as electrode for ORR as well as production of H_2 gas. This gives a motivation to do further studies on this electrode in thin film. Also, double perovskites have a capacity to act as catalyst for OER. Therefore, another series based on PBCO is choose to study as a catalyst for OER.